We are IntechOpen, the world's leading publisher of Open Access books
Built by scientists, for scientists

6,900
Open access books available

186,000
International authors and editors

200M
Downloads

154
Countries delivered to

Our authors are among the
TOP 1%
most cited scientists

12.2%
Contributors from top 500 universities

CLARIVATE ANALYTICS
BOOK CITATION INDEX
INDEXED

WEB OF SCIENCE™

Selection of our books indexed in the Book Citation Index
in Web of Science™ Core Collection (BKCI)

Interested in publishing with us?
Contact book.department@intechopen.com

Numbers displayed above are based on latest data collected.
For more information visit www.intechopen.com

1

Implantable Parylene MEMS RF Coil for Epiretinal Prostheses

Wen Li[1], Damien C. Rodger[2], James D. Weiland[2],
Mark S. Humayun[2], Wentai Liu[4] and Yu-Chong Tai[3]
[1]Michigan State University,
[2]University of Southern California,
[3]California Institute of Technology
[4]University of California, Santa Cruz
USA

1. Introduction

Age related macular degeneration (AMD) and retinitis pigmentosa (RP) are two of the most common outer retinal degenerative diseases that have resulted in vision impairment and blindness of millions of people. Specifically, AMD has become the third leading cause of blindness on global scale, and is the primary cause of visual deficiency in industrialized countries (World Health Organization [WHO], 2011). In the United States, more than 500,000 people are suffering from RP and around 20,000 of them are legally blind (Artificial Retina Project, 2007). Whereas many treatment methods, including gene replacement therapy (Bennett et al., 1996), pharmaceutical therapy, nutritional therapy (Norton et al., 1993), photoreceptor and stem cell transplantations (MacLaren et al., 2006 & Tropepe et al., 2000), and dietary, have been explored to slow down the development of AMD and RP diseases in their early stages, vision impairment and blindness due to outer retinal degeneration currently remain incurable.

In the 1990's, researchers discovered that although the retinal photoreceptors are defective in RP patients, their optic nerves, bipolar and ganglion cells to which the photoreceptors synapse still function at a large rate (Humayun et al., 1999). Further studies showed similar results in AMD patients (Kim et al., 2002). These findings have created profound impact on the ophthalmology field, by providing the possibility of using artificial retinal prostheses to partially restore the lost vision function in AMD and RP patients. Two main retinal implant approaches are currently in development according to the layer of retina receiving the implanted device: subretinal (Chow et al., 2006; Rizzo, 2011; Zrenner et al., 1999) and epiretinal prostheses (Humayun et al., 1994; Weiland & Humayun 2008; Wong et al., 2009). Particularly, epiretinal implantation has received widespread attention over the last few years, for not only successful clinical trials demonstrating its efficacy in patients, but also its many advantages compared to others (Horch K.W. & Dhillon, G.S., 2004). First, the device implantation and follow-up examination only require standard ophthalmologic technologies, which can effectively reduce the risk of trauma during the surgery and also allow for the implant to be replaced easily. In addition, most of the implanted electronics are kept in the vitreous cavity so

that potential thermal damage to the surrounding retinal tissues can be mitigated by taking the advantage of the heat dissipating properties of the vitreous. Finally, developments of modern microelectromechanical systems (MEMS) technologies enable complete intraocular retinal implants and high-density array stimulation.

Various epiretinal prosthetic technique options have been studied by a number of groups worldwide, by replacing the defective photoreceptors with a multielectrode array implanted on the surface of the inner retina between the vitreous and internal limiting membrane (Javaheri et al. 2006; Rizzo et al., 2004; Stieglitz et al. 2004). Although they have different system configurations, these systems generally utilize a pair of coils to transfer data and power wirelessly between an extraocular data acquisition system and intraocular electronics. In such implementations, the intraocular receiver coil, which resides inside the eye, has many constrains compared to the extraocular transmitter coil. First, the coil has to be mechanically durable to withstand the surgical procedure. It also needs to be flexible and small enough to facilitate the device implantation through small incisions. Finally, it should be chemically inert and biocompatible to prevent harmful interaction with surrounding tissue/cells. Currently, most systems are still using thick and stiff hand-wound coils as the receiver coils, which can cause notable degradation in the implant region. In addition, interconnections between the hand-wound coils and other components are usually formed by soldering, which will require additional hermetic package to ensure device biocompability. Planar microcoils that contain electroplated gold wires on flexible polyimide substrates have also been developed (Mokwa et al. 2008). While device functionality has been confirmed in animal models, several critical issues such as long-term reliability and biocompatibility need to be further addressed for human implantation.

To overcome these challenges, we have proposed a polymer-based MEMS technique for making microcoils. Devices typically consist of multi-layer conductive wires encapsulated by polymeric materials (Li et al., 2005; Li et al., 2006; Chen et al., 2008). In this design, Parylene C is selected as a main structural and packaging material because of its many unique properties, such as flexibility (Young's modulus ~ 4 GPa), chemical inertness, United States Pharmacopoeia (USP) Class VI biocompatibility (Rodger et al., 2006), and lower water permeability compared with other commonly used polymers (e.g. PDMS and polyimide) (Licari & Hughes, 1990). Microfabrication technology has several advantages over the hand-winding including miniaturized structures, precise dimensional control, and feasibility for system integration. The proposed coils will finally be integrated with other system components, such as circuitry, discrete electrical components, a flexible cable, and a high-density multielectrode array, to achieve a complete all-intraocular epiretinal prosthetic system (Rodger et al., 2008), as described in Fig. 1.

This chapter will concentrate on the design, microfabrication, and testing results of two types of Parylene-based intraocular MEMS coils for applications in epiretinal implantation. Specifically, Section 2 will introduce theoretical approaches for coil modeling and design. Coil's electrical properties, including self-inductance, effective series resistance (ESR), and parasitic capacitance, will be discussed theoretically with respect to their geometries. Section 3 describes a Parylene-metal-Parylene thin film technology for making the proposed microcoils. Two various types of microfabricated coil prototypes, including regular dual-layered planar coils and novel fold-and-bond coils, are implemented and characterized in Section 4. Successful data transmissions through such devices have been demonstrated using inductive coupling tests. Experiment also confirms that the quality factor (Q factor) of microcoils can increase proportionally with the increase of the number of metal layers.

Preliminary results suggest that the fold-and-bond technology is a very promising approach for making high Q MEMS coils in a simple, low-cost, and microfabrication compatible manner. Future direction for coil optimization will aim to increase the number of metal layers in order to enhance the Q factor and the power transfer efficiency.
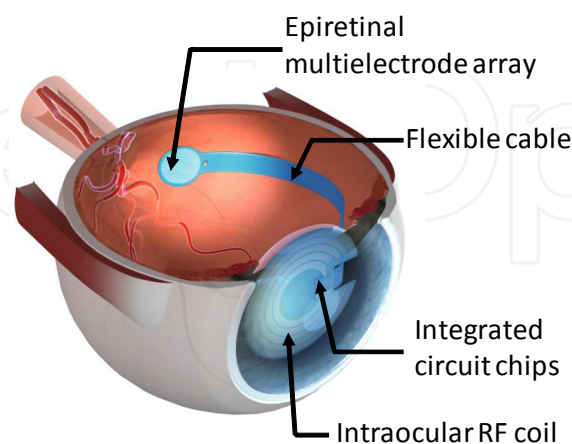

Fig. 1. System schematic of an all-intraocular retinal prosthetic system, which contains two MEMS radio-frequency (RF) coils for power and data transmission, circuitry integrated on a flexible Parylene cable for converting the signal to simulation pulses, and a high-density MEMS electrode array for simulating the neural cells.

2. Modeling of microcoils

Microfabricated coils usually suffer from low self-inductances and inevitable parasitic effects, namely parasitic resistances and capacitances, due to their small physical dimensions and technical constrains of surface micromachining. Particularly, for intraocular retinal implants in human subjects, planar coils with a maximal outer diameter of ~ 10 mm and a minimal inner diameter of ~ 3 mm are desired, which is limited by the space availability in the anterior chamber of human eyes. To better understand the electrical properties and parasitic effects in such small devices, we studied several analytical models and have now applied them to a simplified circular-shape planar coil as illustrated in Fig. 2. In this section, the coil self-inductance, ERS, and parasitic capacitance will be discussed separately with respect to the geometric parameters of devices.
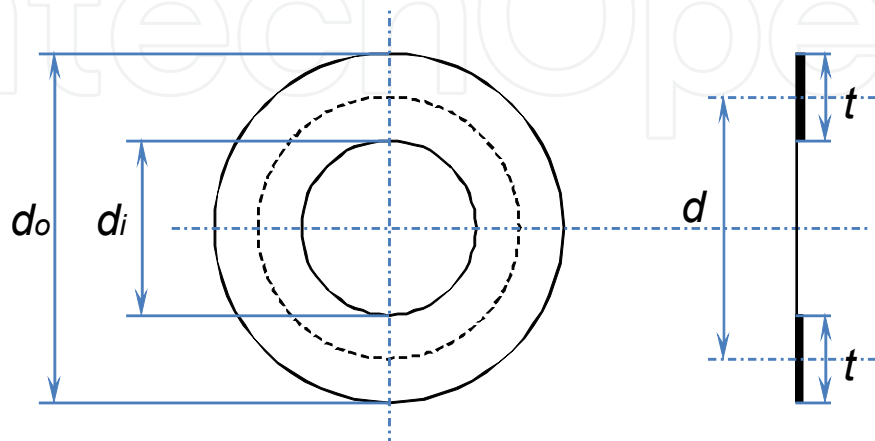

Fig. 2. Simplified model of a circular-shape planar MEMS coil.

2.1 Self-inductance

The self-inductance (L_s) of a multi-layer circular coil with rectangular cross-section can be calculated using the following equation (Dwight , 1945):

$$L_s = 2\pi d(nN)^2 \times 10^{-9} \left[\left(\ln\frac{4d}{t} \right) \left(1 + \frac{t^2}{24d^2} \cdots \right) - \frac{1}{2} + \frac{43t^2}{288d^2} \cdots \right] \quad (\text{in Henry}), \qquad (1)$$

where d (in cm) is the mean diameter of the coil, t (in cm) is the coil width, n is the number of turns on each layer, and N is the total number of layers. This expression is valid only when the coil is operated at a low-frequency, i.e., no skin effect. The skin effect can be evaluated using a frequency-dependent factor, which is known as skin depth δ and can be calculated as

$$\delta = \sqrt{\frac{2\rho}{\omega\mu}} \quad (\text{in meter}), \qquad (2)$$

where ρ is the electrical resistivity of metal (in $\Omega\cdot$m), ω is the angular frequency (in rad/s), and μ is the permeability of metal (in H/m). In our proposed system, the data signal is modulated on a ~ 22 MHz carrier, and the power transfer is taken place at a frequency within 1-2 MHz. Therefore, the estimated skin depths at these low frequencies are much bigger than the thickness of metal thin films produced from physical vapor deposition (PVD). In this case, the skin effect can be negligible with an assumption of uniform current distribution in conductive wires.

2.2 Effective series resistance

ERS (R_s) is commonly used to estimate coil losses, which plays an important role in designing a power efficient inductive link. The ESR can be divided into two parts: DC resistance and frequency dependent resistance. Assuming the width of metal traces is much larger than the separation distance between adjacent turns that can be ignored, the DC resistance of the proposed coil can be calculated with the Ohm's law as given in (3),

$$R_s = \rho \frac{n^2 N\pi d}{t \times h} \quad (\Omega), \qquad (3)$$

where ρ is the metal resistivity (in $\Omega\cdot$m), and h is the metal thickness (in m). As a result of the skin-effect, the frequency dependent part can be neglected at the low operating frequencies as mentioned earlier. Therefore, the equivalent ESR can be simply written as a DC resistance.

2.3 Parasitic capacitance

Parasitic capacitance (C_s) places a limit to the self-resonant frequency of the coil, above which the coil will not behave as an inductor any more. In a first-order approximation, the parasitic capacitance of a planar MEMS coil usually consists of two main components: the capacitance between turns and the capacitance between layers. A distributed model has been developed to estimate the equivalent parasitic capacitance, as discussed elsewhere (Wu et al. 2003 & Zolfaghari et al. 2001). In this method, a planar coil can be decomposed into equal sections by assuming consistent thickness and width of metal traces everywhere. The

voltage profile can then be obtained by averaging the beginning and ending potential across the coil structure. With known voltage variations between the correlated sections of adjacent turns and layers, the total capacitive energy stored in the coil structure can be calculated using the distributed capacitance of each segment. The equivalent capacitance can then be approximated from the distributed capacitances, using the ideal double plate capacitor formula.

$$C_{eq-turn} = \sum_{k=1}^{n-1} \frac{1}{4} C_{ii} l_k [d(k+1) - d(k-1)]^2, \tag{4}$$

$$C_{eq-layer} = \frac{1}{4} \sum_{k=1}^{N} (C_{m,m-1} + C_{m-2,m-3} + ...) \frac{A_k}{m^2} [4 - 2d(k-1) - 2d(k)]^2$$
$$+ \frac{1}{4} \sum_{k=1}^{N} (C_{m-1,m-2} + C_{m-3,m-4} + ...) \frac{A_k}{m^2} [2d(k-1) + 2d(k)]^2, \tag{5}$$

$$C_{eq-total} = C_{eq-turn} + C_{eq-layer}, \tag{6}$$

Equations (4), (5), and (6) show the analytical formulas for calculating parasitic capacitance, where C_{ii} (in F) denotes the capacitance per unit length between adjacent metal turns, $C_{m, m-1}$ (in F) is the capacitance per unit area between the m-th and (m-1)-th metal layer, A_k (in m^2) is the trace occupied area of the k-th turn on each layer, and $d(k) = h_1 + h_2 + ... + h_k$, in which h_k is defined as the ratio of the wire length of the k-th turn (l_k) to the total wire length (l_{tot}). This simplified model neglects the second order parasitic capacitances between non-adjacent turns and layers, which are much less than the first order capacitances.

2.4 Quality factor

Q factor is an important metric for evaluating the efficiency of a coil, which is theoretically defined as the ratio of total stored energy to dissipated energy per cycle in a resonating system. With known L_s, R_s, and C_s, the Q factor of the coil can be derived from a 3-element circuit model (Fig. 3) (Wu, 2003). In order to obtain the coil Q factor mathematically, the total equivalent impedance (Z_s) is first studied, which can be written as the sum of a real resistance and an imaginary reactance (equation [7]).
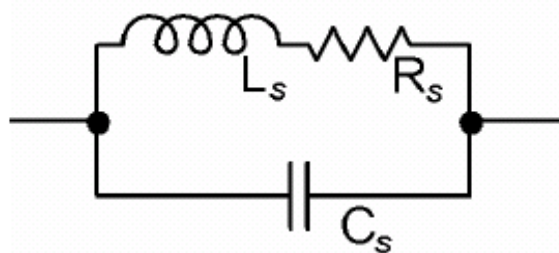

Fig. 3. Equivalent RLC circuit of a planar MEMS coil.

$$Z_s = \frac{R_s}{(1 - \omega^2 L_s C_s)^2 + (\omega C_s R_s)^2} + j \frac{\omega(L_s - R_s^2 C_s - \omega^2 L_s^2 C_s)}{(1 - \omega^2 L_s C_s)^2 + (\omega C_s R_s)^2}. \tag{7}$$

Then the self-resonant frequency ω_s can be expressed as:

$$\omega_s = \sqrt{\frac{1}{L_s C_s} - \frac{R_s^2}{L_s^2}} \approx \sqrt{\frac{1}{L_s C_s}}, \text{ when } R_s \ll \sqrt{\frac{L_s}{C_s}}. \tag{8}$$

For a retinal implant system, when both the external and internal units of the inductive link are tuned to a same resonant frequency ω_r, the maximal coupling energy can be delivered to the implanted system. In this case, the coil Q factor can be expressed with the following equation:

$$Q_r = \frac{Im(Z_s)}{Re(Z_s)} \approx \frac{\omega_r L_s}{R_s} \tag{9}$$

Combining with equations (1) and (3), equation (9) can be rewritten as

$$Q_r = \frac{2\omega_r N t h}{\rho}\left[\left(\ln\frac{4d}{t}\right)\left(1+\frac{t^2}{24d^2}\cdots\right) - \frac{1}{2} + \frac{43t^2}{288d^2}\cdots\right] \times 10^{-9} \tag{10}$$

Ideally, the Q factor of a coil should be as high as possible in order to minimize the power loss in the device as well as to maximize power transfer efficiency of the system. It can be seen from equation (10) that Q_r can be enhanced by increasing the number of coil layers (N), the coil width (t), and/or the thickness of the conductive layer (h). For an intraocular retinal implant, however, there is not much zoom to improve the coil width due to the small coil dimensions (inner diameter, outer diameter, etc.) confined by the eyeball size. Therefore, a more applicable way to increase a coil's Q factor is to increase the number of stacking layers as well as the thickness of conductive wires.

2.5 Finite element simulation

To validate the effectiveness of the theoretical models, finite element simulations (FES) are performed using a built-in package in CoventorWare (Coventor Inc., Cary, NC). As a demonstration, a coil with two layers of metal is designed, and its electrical characteristics are evaluated using both analytical models and FES, as summarized in Fig. 4 and Table 1.

During the simulation, an octagonal coil is used to approximate a circular shape due to memory constraint in CoventorWare. The coil self-inductance and the ESR are simulated over a frequency range from 10 kHz to 1 GHz. It can be seen that the self-inductance at 1 MHz shows only 2.2% deviation, and the ESR deviates by less than 6%, suggesting good agreement with the analytical models. The slight deviations might be introduced by the approximation of coil shape. Note that L_s and R_s both remain stable at frequencies below 10 MHz, indicating that skin effect or proximity effect is negligible at target frequencies of 1 or 2 MHz.

	OD (mm)	ID (mm)	Trace cross section (μm × μm)	Number of turns	L_s (μH)	R_s (Ω)	C_s (nF)	Q at 1MHz
Calculations	10	3	220 × 2	28 / Layer	5.0	28.9	65.5	1.1
FES	10	3	220 × 2	28 / Layer	4.9	27.4	--	1.12

Table 1. Coil characteristics estimated using both analytical models and FES.
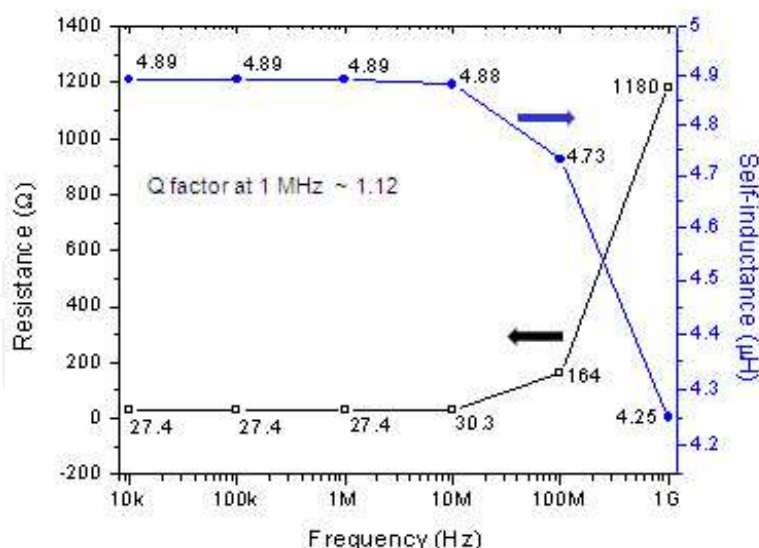
Fig. 4. Simulated self-inductance and ESR of the sample coil.

3. Parylene-metal-Parylene thin film technology

A multi-layer Parylene-metal thin film technology for making the proposed microcoils has been developed (Li et al., 2005). In this approach, thin-film metal conductive wires are sandwiched between multiple layers of Parylene C and interconnections between two adjacent layers are implemented using through holes in the Parylene insulation layer. Fig. 5 depicts a typical process flow for making a dual-metal-layer structure. Briefly, a layer of sacrificial photoresist is optionally spun on a standard silicon wafer, followed by Parylene C deposition (PDS 2120 system, Special Coating Systems, Indianapolis, IN, USA) (*Step 1*). A layer of metal is then deposited on top of the Parylene using an electron beam (e-beam) evaporator (SE600 RAP, CHA Industries, Fremont, CA, USA), and patterned using a wet etching process (*Step 2*). After that, a thin layer of Parylene C is deposited as an insulation layer between two metal layers, and the interconnection vias are selectively opened with oxygen plasma in a reactive ion etch system (RIE) (Semi Group Inc. T1000 TP/CC) using a photoresist mask(*Step 3*). After removing the photoresist mask, the second metal layer is evaporated and patterned, followed by another Parylene C deposition to conformally cover the exposed metal wire (*Step 4*). A photoresist mask is then patterned to expose the contact pads, as well as to define the coil shape (*Step 5*). Finally, oxygen plasma etch is performed to remove unwanted Parylene C, and the entire flexible device is released from the silicon substrate by dissolving the sacrificial photoresist (*Step 6*).

The reliability of the interconnections between nearby metal layers highly depends on the step coverage of the Parylene sidewall during metal evaporation, which can be improved by a slightly isotropic O_2 plasma etch (Meng et al., 2008). A special design of rotating wafer holder inside the e-beam evaporator also helps adjust the angle of attack of metal evaporant for best coverage. Microcoils comprising more than two layers of metal can be fabricated with similar procedure by alternating the Parylene C deposition, interconnection via fabrication, and metal evaporation process steps. Although it is specifically developed for microcoil fabrication, this technology can also be applied to the fabrication of other flexible, implantable devices with multi-layer Parylene-metal structures, such as dual-metal-layer electrode arrays (Rodger et al., 2008).
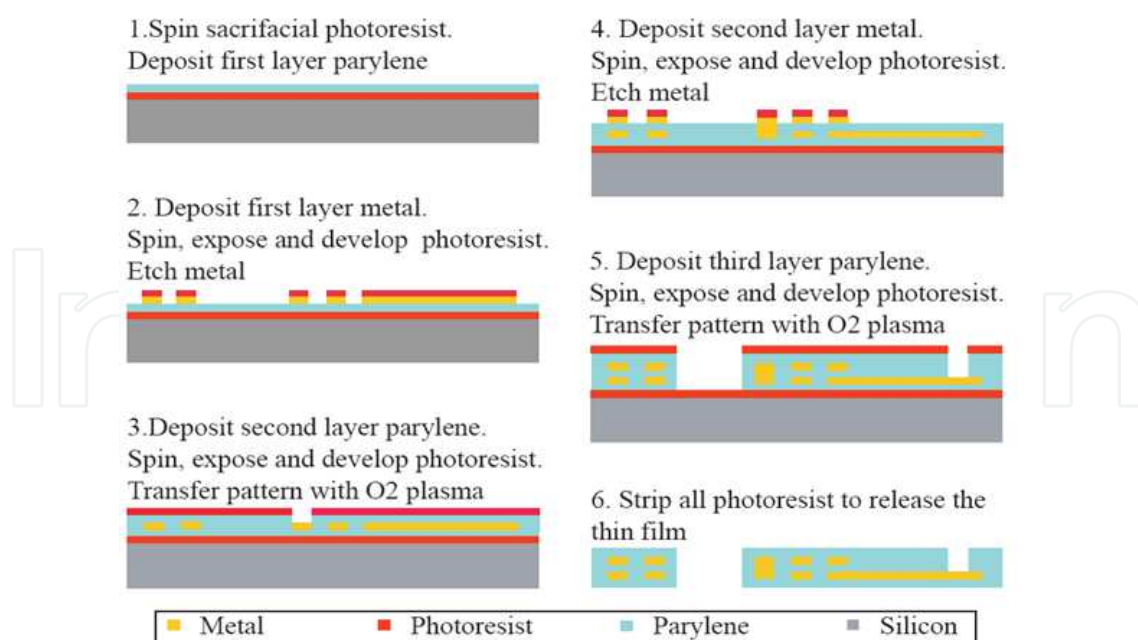
Fig. 5. Fabrication process flow of a dual-metal-layer Parylene-based MEMS structure.

For implantable devices, our Parylene-metal thin film technology has several unique advantages compared with conventional semiconductor-based microfabrication technologies. Using biocompatible Parylene directly as the actual substrate greatly simplifies the device integration and packaging procedures. Devices fabricated in this way are very flexible and foldable so that they can be implanted through small surgical incisions, allowing wounds to heal quickly. Moreover, the metal lines are completely padded by the Parylene material, and can therefore withstand repeated bending during surgical handling. Finally, a post-fabrication heat-molding process has been developed to modify the skins into various shapes that match the curvatures of the target implant areas (Tai et al., 2006).

4. Coil designs and fabrication results

4.1 Dual-layered MEMS coil
In this section, a planar coil is designed, which features: 1) dual-layer thin-film metal conductive wires sandwiched between multiple layers of Parylene C, and 2) interconnections between two adjacent layers that are formed by filling the Parylene through holes with PVD metal. Fig. 6 shows the microscope images of a fabricated coil and its interconnection via. This coil has totally 10 turns of wires made of approximately 2000 Å multiple layers of Ti/Au/Ti metallization. Titanium serves as an adhesion promoter to improve the bonding strength between gold and Parylene C. The device has overall dimensions of ~ 9.5 mm in outer diameter, ~ 5 mm in inner diameter, and ~ 11 µm in thickness, limited by the lens capsule size of the human eyes. The interconnection via occupies an area of ~ 0.06 mm² with a contact resistance of less than 1 Ω, which can be negligible compared with the total coil ESR. The device is proven to be very flexible and foldable (Fig. 7), easing the procedure of surgical insertion and lessening physical damages in the region of implantation.
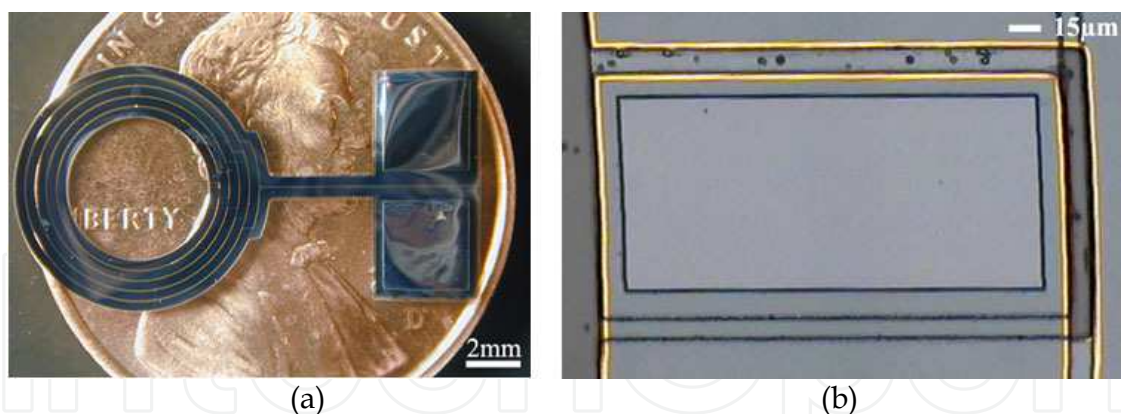
Fig. 6. (a) A fabricated dual-metal-layer coil sitting on a penny. (b) The microscope image shows the interconnection via between two metal layers. (Li et al., @ 2005 IEEE)

Fig. 7. Demonstration of the coil's flexibility and foldability. (Li et al., @ 2005 IEEE)

The electrical properties of the fabricated coil are characterized experimentally. Recall equation (7) in Section 2, by setting the derivation of the real part to zero and equating the imaginary part to zero, the self-inductance (L_s) and the parasitic capacitance (C_s) can be extracted using equations (11) and (12), where ω_0 is defined as the frequency at which the real part of the impedance is maximum, and ω_z is the zero-reactance frequency at which the imaginary part of the impedance is zero (Wu, 2003).

$$L_S = \frac{R_s}{\sqrt{2(\omega_0^2 - \omega_z^2)}},$$ (11)

$$C_S = \frac{\sqrt{2(\omega_0^2 - \omega_z^2)}}{R_s(2\omega_0^2 - \omega_z^2)}.$$ (12)

For the coil in Fig. 6, the ESR (R_s) is measured to be around 72 Ω and the resistivity of e-beam deposited gold is calculated to be around 2.25×10^{-6} Ω·cm. This number agrees with the resistivity of bulk gold (2.2×10^{-6} Ω·cm), implying that the E-beam evaporated metal is void-free. The coil impedance is swept with an HP 4192A LF impedance analyzer over a frequency range from 5 Hz to 13 MHz. From the impedance versus frequency curves (Fig. 8), f_0 and f_z can be read with values of 7.5 MHz and 3.3 MHz respectively. Knowing R_s, ω_0, and ω_z, the coil self-inductance and capacitance are therefore calculated as $L_s = 1.19$ µH and

C_s = 201 pF. The theoretical numbers are also calculated using the abovementioned equations, and the fitting curves are plotted in Fig. 8, in comparison with the measured curves. The experimental data matches the theoretical calculations closely, with deviations of less than 19%. These errors may be attributed to the simplification of the 3-element model as well as interferences from the measurement instruments. The Q factor of the coil is obtained to be approximately 0.1 at the target frequency of 1 MHz, as expected from the design.
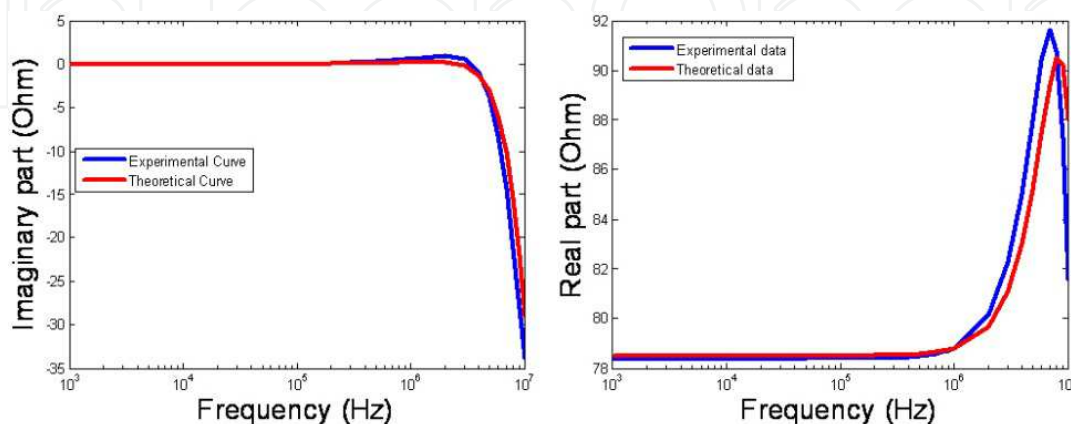
Fig. 8. Impedance measurement and curve fitting using the 3-element model: (a) Imaginary part; (b) Real part. (Red curves correspond to theoretical parameters of the fabricated coil: L_s = 1.0 μH, R_s = 67 Ω and C_s = 183 pF.)

The data and power transfer performances have also been verified using a custom designed data link at the University of California, Santa Cruz (UCSC). The testing waveforms are shown in Fig. 9, where the blue curve represents the data driving signal on the primary stage, the green curve represents the voltage across the primary coil, and the purple curve represents the receiving voltage across the secondary coil.
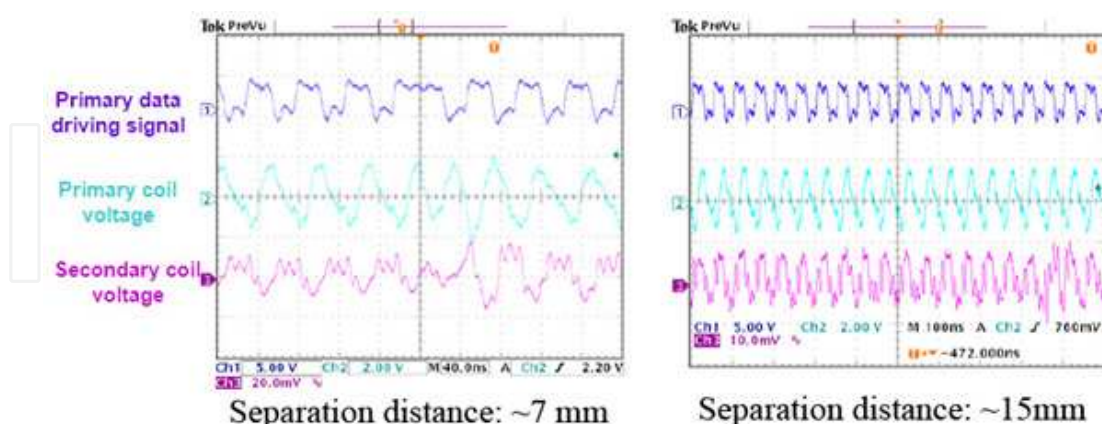

Fig. 9. Inductive coupling test waveforms: (a) received signal is 25 mV peak to peak; (b) received signal is 15 mV peak to peak.

While successful data transmission through our coils has been demonstrated, it is noted that this device has no driving capability due to its small Q factor (~ 0.1), meaning that the power cannot be delivered to the load. Therefore, enhancing coil's Q factor to achieve a higher power transfer efficiency is crucial for designing the next generation of coils.

Experiments have been done at UCSC to study the feasibility of using MEMS coils as the receiver coil for the current inductive link design. A rough estimate is that, in the worst case, a minimal Q factor of 10 will be needed in order to deliver ~100 mW for chip operation and stimulation. From the theoretical analysis herein, it is known that the Q factor can be enhanced by increasing the metal thickness and/or the number of metal layers. However, e-beam evaporated metals are usually limited in film thickness due to high process cost. Electroplated and sputtered metals can be thicker alternatives but their qualities, such as density and conductivity, are typically not as good as evaporated metals. This problem becomes more serious especially when devices are implanted inside harsh biological environments. From the device design aspect, increasing metal layers is more practical for the Q factor enhancement of MEMS coils, thus a fold-and-bond technology emerges as a good candidate.

4.2 Fold-and-bond coil

In the concept of fold-and-bond technology (Fig. 10), two or more thin-film planar spiral coil segments are fabricated from the same batch so that each segment has identical self-inductance and ESR, denoted by L_s and R_s, respectively. A new coil can then be formed by stacking n segments together in either parallel or series connections. For parallel stacking, particularly, the new coil will have identical inductance but n-times larger in equivalent metal thickness, resulting in an n-times lower ESR. As for series stacking, the resistance remains the same while the inductance increases by n-times because of the mutual inductance between adjacent layers. According to the definition of the Q factor, both approaches can achieve an n-times Q factor enhancement. In this section, the series stacking configuration is used to demonstrate the technology concept.

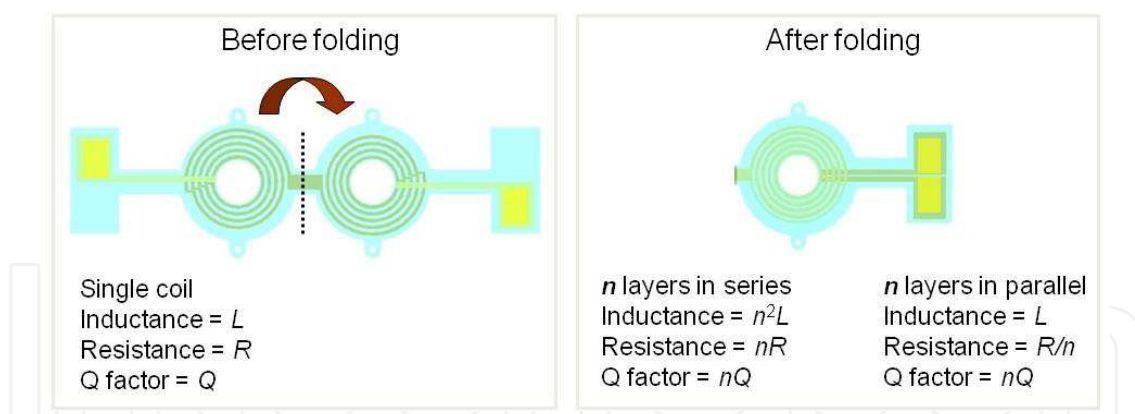| Before folding	After folding
Single coil Inductance = L Resistance = R Q factor = Q	n layers in series Inductance = n^2L Resistance = nR Q factor = nQ

Fig. 10. Concept of the fold-and-bond technology for Q factor enhancement.
A coil with one fold is depicted for representation.

Fold-and-bond coil's fabrication involves the dual-metal-layer Parylene/metal skin realization and a post-fabrication thermal bonding process (Li et al., 2008). The Parylene-metal skin with two buried layers of metal is first fabricated in the same manner as described in Fig. 5, in which one layer of metal is used to form the conductive wires of the coil, while the other layers is used to make the interconnections between the layers. This thin film skin can be folded and stacked into multiple layers because of the flexibility of Parylene C. While hand alignment under an optical microscope is used at the current stage, special alignment jigs can be custom designed in the future to achieve precise

alignment of different layers. During the thermal bonding procedure, the folded device is sandwiched between two glass slides covered with aluminum sheets, which can avoid Parylene sticking on the glass. The whole unit is placed in a vacuum oven and bonded at 230 °C for two days. External pressure can be applied as needed to enable Parylene-Parylene bonding at moderate temperatures. The vacuum pressure is controlled at ~ 10 Torr to prevent Parylene C from unwanted oxidation in air at an elevated temperature.

Two Parylene-based skins with dual-layer embedded metal have been fabricated, as shown in Fig. 11. These prototypes are specifically designed for intraocular retinal prosthesis with the design parameters described in Table 2. The thickness of metal wires is increased to ~ 2 μm in order to further reduce the coil's DC resistance. The metal is covered with ~ 3.4 μm Parylene C on each side with the lead contact vias open. Fig. 12 shows the final devices after folding and thermal bonding. Misalignments of 10 μm to 30 μm have been observed, which is due to the lack of control with the hand alignment.

Type	Total number of turns	R_s (Ω)	L_s (μH)	C_s (pF)	Q at 1MHz
I	28	29	2.9	65.5	1.1
II	48	90	14.8	64.5	1

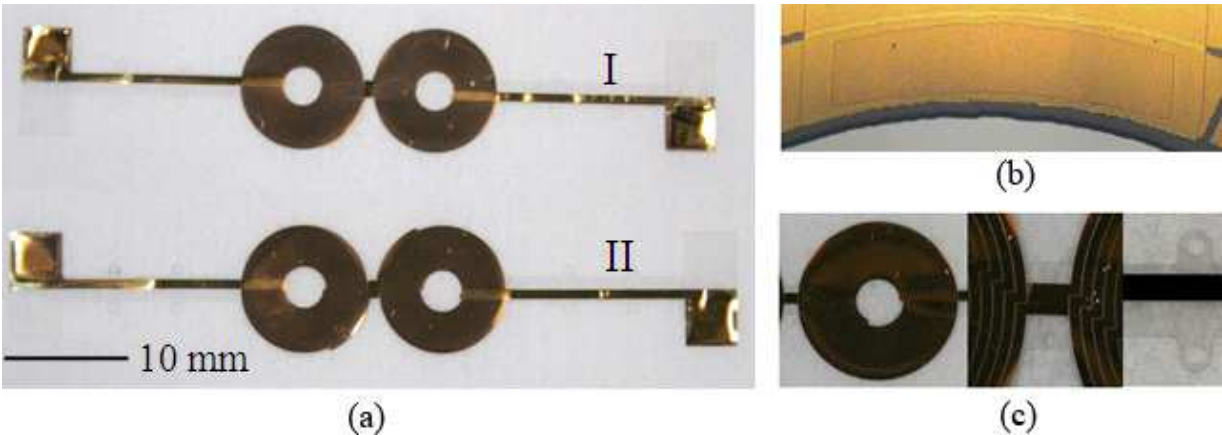Table 2. Design specifications of two fold-and-bond coils.

Fig. 11. Devices before thermal bonding: (a) Fabricated dual-metal-layer Parylene-based skins; (b) Microscope image of an interconnection via between two metal layers; (c) Photos of device details (from left to right): conductive wires of the coil, folding junction and suturing holes.

The devices still remain flexible after bonding (Fig. 13 (a)), indicating that annealing at a temperature below the melting point of Parylene C (290 °C) (Harder et al. 2002) will not alter the mechanical flexibility of the material. The DC resistances of the samples are measured before and after bonding with no significant change observed (Table 3), confirming the ductility and durability of metal traces. Stretching marks and Parylene cracks are found along the folding line after thermal treatment, which is caused by stress concentration during folding. Additional Parylene coating can be performed after thermal bonding to conformally cover these cracks in order to ensure a good sealing for final devices.
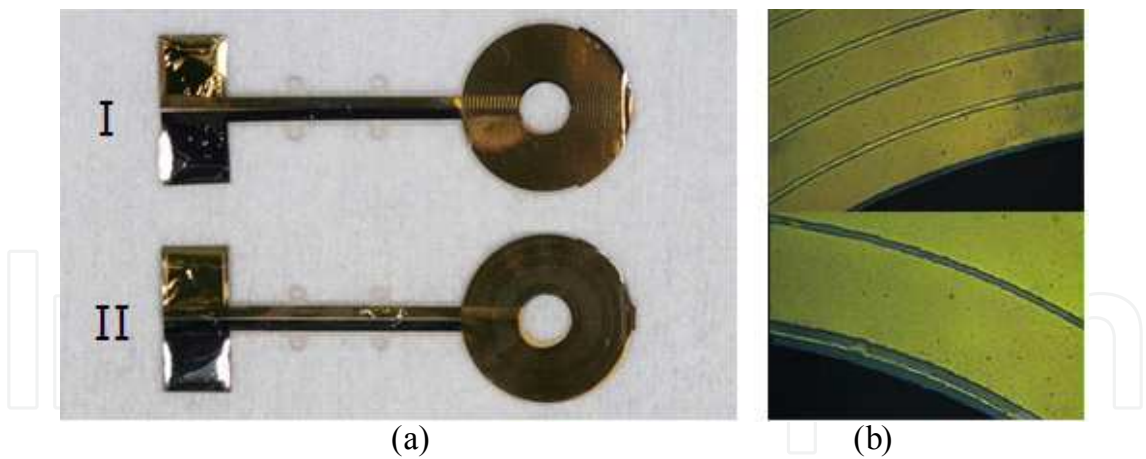
Fig. 12. Devices after thermal bonding: (a) Fold-and-bond coils after thermal bonding. (b) Overlapping metal wires with misalignments of 10 μm to 30 μm.
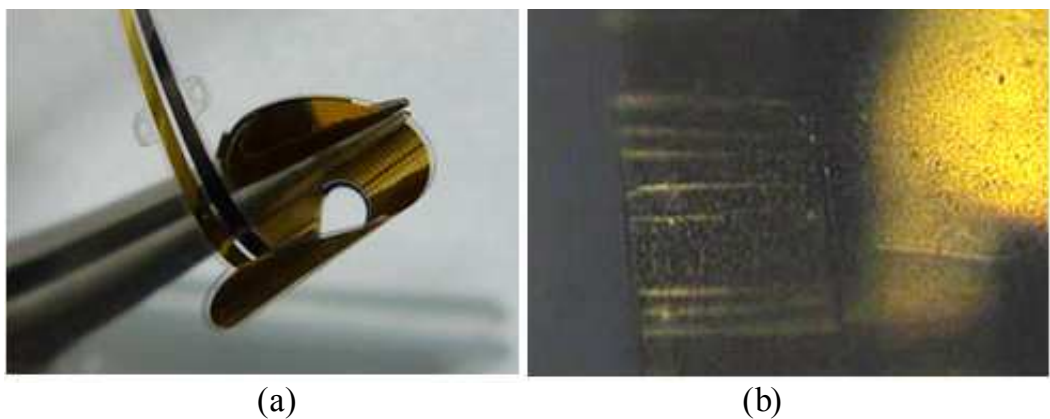

Fig. 13. (a) Demonstration of device's flexibility; (b) Stretching marks along the folding line.

The electrical characteristics of the fabricated fold-and-bond coils are studied before and after thermal bonding. The lump parameters are extracted from the same 3-element model, as summarized in Table 3. As expected, the self-inductance and Q-factor of the coil are increased by more than 90% for both coil designs after folding. Changing the wire width has no significant impact on the parasitic capacitance, indicating the capacitance between adjacent layers is dominant over the capacitance between turns. Coil prototype I shows a much higher ESR compared to its theoretical value (29 Ω), which may be attributed to the non-uniformity of metal thickness. Overall, the measured values show good agreement with the theory predictions, demonstrating that the theoretical model can predict the coil properties effectively.

Type		R_s (Ω)	L_s (μH)	C_s (pF)	Calculated Q at 1MHz	Q Increase
I	Before	41.2	2.9	--	0.44	--
	After	41.8	5.7	62.1	0.85	95%
II	Before	91.3	8.6	--	0.58	--
	After	92.2	16.3	70.8	1.11	91%

Table 3. Measured electrical parameters of fold-and-bond coils using the 3-element model.

To study the power transfer efficacy, the fabricated devices are tested using a simplified inductive link, as shown in Fig. 14. In this setup, the transmitter coil is hand-wound with a self-inductance of ~ 23 μH and a series resistance of ~ 1.5 Ω. The inner diameter of the transmitter coil is optimized to be ~ 30 mm (Ko et al., 1977). The receiver coil is the fold-and-bond coil presented in Fig. 12. During the measurements, the primary stage is driven by an HP E3630A function generator with a sinusoidal input signal of 20 V peak to peak. Both the primary and secondary circuits are subject to parallel resonance with the same resonant frequencies of ~ 1 MHz. To minimize environmental interferences, both the transmitter and receiver coils are covered with aluminum foils as electromagnetic shielding.
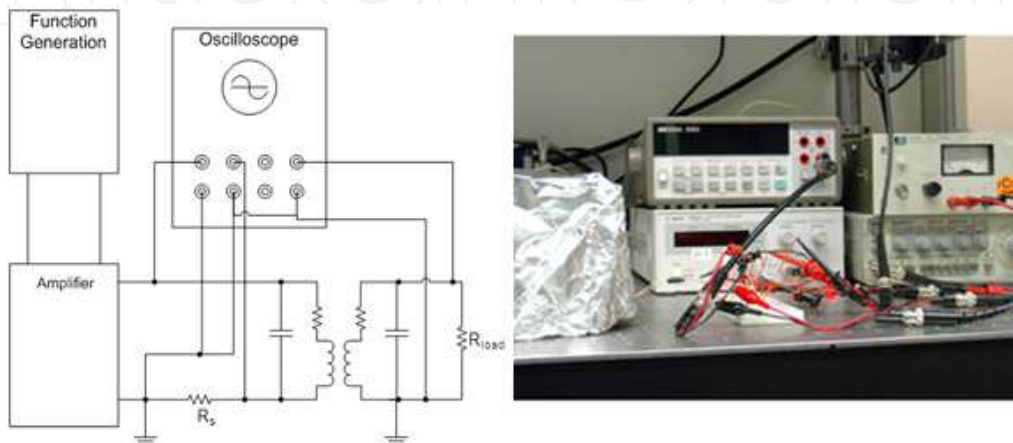
Fig. 14. Experimental setup of power transmission measurement and its circuit diagram.

Preliminary experiments have been performed. A 10 Ω series resistor (R_s) is incorporated in the primary stage to monitor the output current from the amplifier. The voltage across the transmitter coil is then calculated by subtracting the resistor voltage from the output voltage of the amplifier. The transferred power, which is defined as the power delivered to a 1 kΩ load resistor (R_{load}), can be obtained by directly measuring the voltage across the load resistor. The power transfer efficiency of two coil prototypes, which is calculated as the ratio of the transferred power to the total output power from the amplifier, is plotted in Fig. 15, as
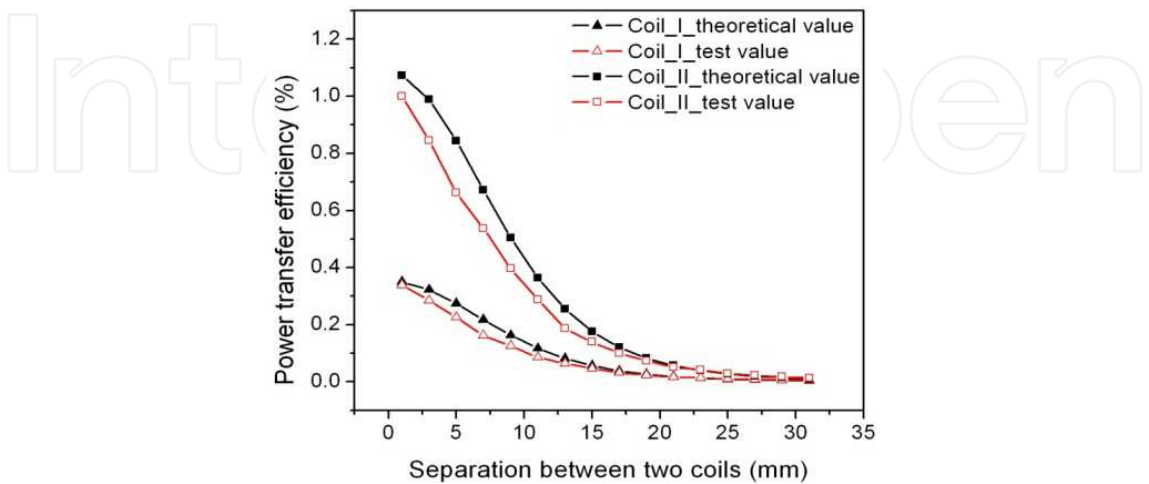

Fig. 15. Power transfer efficiencies of the fold-and-bond coils at 1 MHz, as functions of separation distances of the coil pair.
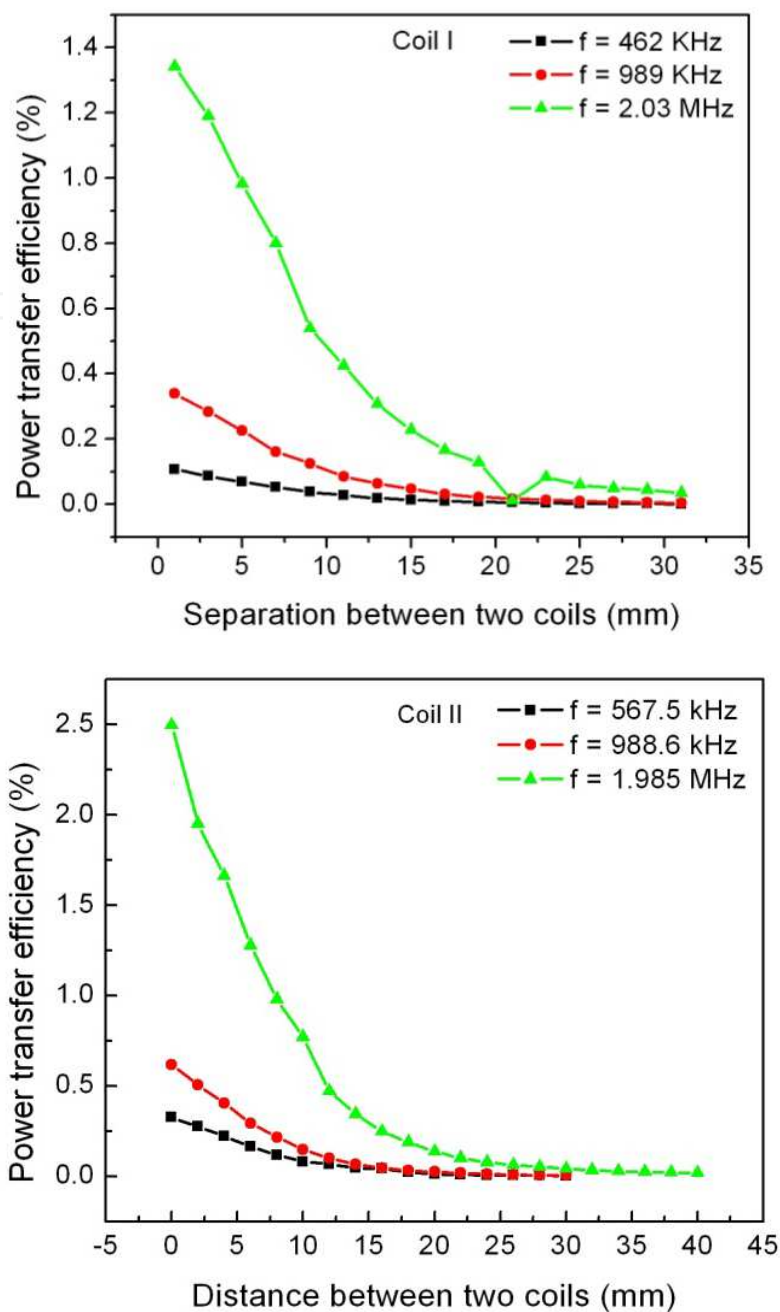
Fig. 16. The power transfer efficiency of difference devices vs. the separation distance of the coil pair.

functions of the separation distance between the coil pairs. For comparisons, theoretical data are also studied based on the models discussed elsewhere (Ko et al., 1977), which match the testing results within a reasonable range. As expected, the coil prototype II with higher self-inductance and Q factor exhibits higher power transfer efficiency at the same separation distances. The power transfer efficiencies at different operation frequencies have also been investigated, as plotted in Fig.16. The results show that the power transfer efficiency can be enhanced by more than 3 times when the operation frequency is changed from ~1 MHz to ~2 MHz. This can be attributed to the effective Q factor increases by almost two times as the frequency goes up.

Nevertheless, the power transfer efficiency of the current coil prototypes is still below 0.4% at the target implantation depth of ~ 15 mm, which is insufficient to drive electronics for high-density retinal stimulation. Whereas more power can be generated from the primary stage to compensate the low efficiency, the overheating issue of the coils becomes prominent. Therefore, future direction for coil optimization will mainly focus on increasing the number of metal layers to improve the Q factor. Theoretical evaluation predicts that at least 20 layers of metal will be required in order to achieve a reasonable Q factor of around 10, with a given gold thickness of ~ 2 μm.

4.3 Challenges in packaging

Device packaging for retinal prostheses presents several challenges. Electrical and fluidic isolation must be maintained to avoid device failures upon exposure to corrosive eye fluid. To ensure long-term use of implants, the interface between device and biological tissues should be stable and biocompatible in order to minimize inflammation and immune response. Packaging complication is also one of the significant challenges for high-density neural simulation/recording. Careful selection and evaluation of packaging materials and tools are necessary to address such challenges. We have studied the packaging performance of Parylene C using accelerated lifetime soak testing in heated saline. Preliminary results estimate that the lifetime of Parylene-coated metal at body temperature (37 °C) is more than 60 years, suggesting good packaging performance of Parylene C. Experimental details on Parylene packaging evaluation are discussed elsewhere (Li et al., 2010).

A chip-level integrated interconnect (CL-I²) packaging method has also been explored for integration of microcoils with CMOS integrated circuit (IC) chips and high-density prosthetic electrodes (Rodger et al., 2005 & Li et al. 2010). In this method, all the IC components necessary for a retinal implant can be embedded in silicon cavities and functional Parylene-based MEMS devices (e.g. microcoil and high-density electrode array) can then be fabricated on the same platform using the abovementioned Parylene-metal thin film technology. Chip-to-microdevice interconnections can be constructed using standard microfabrication techniques such as photolithography and metal etching; therefore, eliminating wire-bonding, bump-bonding, or soldering steps. Whereas initial experiments show promising results, continuous investigations will be necessary to collect more data in order to optimize integration process and to further refine our knowledge of Parylene packaging behavior.

5. Conclusion

In this work, various types of MEMS coils have been designed and fabricated using the Parylene-metal-Parylene skin technology. Experiments have been performed to measure the electrical properties of the coils and the results show good agreement with the theoretical values. The data transfer effect has been successfully demonstrated with the telemetry link setup. However, the power transfer efficiency at the separation distance of 15 mm is below 0.4%, which is relatively low for high-density retinal stimulation. Given the constraints of device geometries, it is believed that increasing the number of metal layers will be the most effective and applicable way to enhance the Q factor of microcoils. According to the analytical models, at least 20 layers of metal will be needed in order to achieve a coil Q

factor of approximately 10. While direct fabrication could be too complicated to be carried out, the fold-and-bond technology has proven itself as a very promising fabrication technology. Although specifically tailored to the needs of retinal prostheses, because our coils are fully micromachined in a way compatible with multielectrode arrays and the Parylene-based embedded chip packages, these devices can be easily integrated with various system components to achieve a new range of true system solutions for both biomedical and non-biomedical applications.

6. Acknowledgment

## 7. References

Artificial Retina Project. (2007). Retinal Diseases: Age-Related Macular Degeneration and Retinitis Pigmentosa. Available from
http://artificialretina.energy.gov/diseases.shtml.

Bennett, J.; Tanabe, T.; D. Zeng, Sun, Y.; Kjeldbye, H.; Gouras, P. & Maguire, A.M. (1996). Photoreceptor Cell Rescue in Retinal Degeneration (RD) Mice by In Vivo Gene Therapy. *Nature Medicine*, Vol. 2, (June 1996), pp. 649-654, ISSN 1078-8956.

Chen, P.J.; Kuo, W.C.; Li, W. & Tai, Y.C. (2006) Q-enhanced Fold-and-bond MEMS Inductors. *Proc. IEEE Int. Conf. on Nano/Micro Engineered and Molecular Systems*, ISBN 978-1-4244-1907-4, Sanya, Hainan Island, China, January 2008.

Chow, A.Y.; Chow, V.Y.; Packo, K.H.; Pollack, J.S.; Peyman, G.A. & Schuchard, R. (2006). The Artificial Silicon Retinamicrochip for the Treatment of Vision Loss from Retinitis Pigmentosa. *Arch Ophthalmol*, Vol. 122, (April 2004), pp. 460-469, ISSN 0003-9950.

Dwight, H.B. (1945). *Electrical Coils and Conductors*, McGraw-Hill, ASIN B0007IT6Z0, New York, United States.

Harder, T.; Yao, T.J.; He, Q.; Shih, C. Y. & Tai, Y.C. (2002). Residual Stress in Thin-film Parylene C. *Proc. IEEE Int. Conf. on Micro Electro Mechanical Systems*, ISBN 0-7803-7185-2, Las Vegas, United States, January 2002.

Horch K.W. & Dhillon, G.S. (2004). *Neuroprosthetics Theory and Practice (Series in Bioengineering & Biomedical Engineering-Vol.2)*, World Scientific Publishing Company, ISBN 9812380221, Singapore.

Humayun, M.S.; Propst, R.; Eugene de Juan Jr.; McCormick, K. & Hickingbotham, D. (1994). Bipolar Surface Electrical Stimulation of the Vertebrate Retina. *Arch Ophthalmol*, Vol. 112, (January 1994), pp. 110-116, ISSN 0003-9950.

Humayun, M.S.; Eugene de Juan Jr.; Weiland, J.D.; Dagnelie, G.; Katona, S.; Greenberg, R. & Suzuki, S. (1999). Pattern Electrical Stimulation of the Human Retina. *Vision Research*, Vol. 39, (July 1999), pp. 2569-2576, ISSN 0042-6989.

Javaheri, M.; Hahn, D.S.; Lakhanpal, R.R.; Weiland, J.D. & Humayun, M.S. (2006). Retinal Prostheses for the Blind. *Ann Acad Med,* Vol. 35, (March 2006), pp. 137-144, 2006, ISSN 0304-4602.

Kim, S.Y.; Sadda, S.; Pearlman, J.; Humayun, M.S.; Eugene de Juan Jr. & Green, W.R. (2002). Morphometric Analysis of the Macula in Eyes with Disciform Age-realted Macular Degeneration. *Retina*, Vol. 22, No. 4, (August 2002), pp. 471-477, ISSN 0275-004X.

Ko, W.H.; Liang, S.P. & Fung, C.D.F. (1977). Design of Radio-frequency Powered Coils for Implant Instruments. *Med. Bio. Eng. Comput.*, Vol. 15, (November 1977), pp. 634-640, ISSN 0140-0118.

Li, W.; Rodger, D.C.; Weiland, J.D; Humayun, M.S. & Tai, Y.C. (2005). Integrated Flexible Ocular Coil for Power and Data Transfer in Retinal Prostheses. *Proc.27th Ann. Int. IEEE-EMBS Conf.*, ISBN 0-7803-8741-4, Shanghai, China, January 2005.

Li, W.; Rodger, D.C.; Meng, E.; Weiland, J.D.; Humayun, M.S. & Tai, Y.C. (2006). Flexible Parylene Packaged Intraocular Coil for Retinal Prostheses. *Proc. 4th Int. IEEE-EMBS Special Topic Conf. on Microtechnologies in Medicine and Biology*, ISBN 1-4244-0338-3, Okinawa, Japan, May 2006.

Li, W.; Rodger, D.C. & Tai, Y.C. (2008). Implantable RF-coiled Chip Packaging. *Proc. IEEE Int. Conf. on Micro Electro Mechanical System*, ISSN 1084-6999, Tucson, United States, January 2008.

Li, W.; Rodger, D. C.; Meng, E.; Weiland, J. D.; Humayun, M. S. & Tai, Y.-C. (2010) Wafer-Level Parylene Packaging with Integrated RF Electronics for Wireless Retinal Prostheses. *Microelectromechanical Systems, Journal of*, Vol. 19, (June 2010) pp. 735-742, ISSN 1057-7157.

Licari J. J. & Hughes, L. A. (1990). *Handbook of Polymer Coating for Electronics: Chemistry, Technology, and Applications*, William Andrew Publishing/Noyes, ISBN 081551235X, Park Ridge, New Jersey, United States.

MacLaren, R.E.; Pearson, R.A.; MacNeil, A.; Douglas, R.H.; Salt, T.E.; Akimoto, M.; Swaroop, A.; Sowden, J.C. & Ali, R.R. (2006). Retinal Repair by Transplantation of Photoreceptor Precursors. *Nature*, Vol. 444, (November 2006), pp. 203-207, ISSN 0028-0836.

Meng E., Li P.Y. & Tai, Y.C. (2008) Plasma Removal of Parylene C, *Journal of Micromechanics and Microengineering,* Vol 18, (February 2008), pp. 045004, ISSN 1361-6439.

Mokwa, W.; Goertz, M. C.; Krisch, K. I.; Trieu, H.-K. & Walter, P. (2008) Intraocular Epiretinal Prosthesis to Restore Vision in Blind Humans. *Proc. 30th Ann. Int. IEEE EMBS Conf.*, ISBN 978-1-4244-1814-5, Vancouver, British Columbia, Canada, August 2008.

Norton, E.W.D.; Marmor, M.F.; Clowes, D.D.; Gamel, J.W.; Barr, C.C.; Fielder, A.R.; Marshall, J.; Berson, E.L.; Rosner, B.; Sandberg, M.A.; Hayes, K.C.; Nicholson, B.W.; Weigel-DiFranco, C.; Willett, W.; Felix, J.S. & Laties, A.M. (1993). A Randomized

Trial of Vitamin A and Vitamin E Supplementation for Retinitis Pigmentosa. *Arch Ophthalmol*, Vol. 11, (June 1993), pp. 1460-1466, ISSN 0003-9950.

Rizzo, J.F.; Wyatt, J.L.; Loewenstein, J.; Montezuma, S.; Shire, D.B.; Theogarajan, L. & Kelly, S.K. (2004). Development of a Wireless, Ab Externo Retinal Prosthesis. *Invest Ophthalmol Vis. Sci.*, Vol. 45, pp. 3399.

Rizzo, J.F. (2011). Update on Retinal Prosthetic Research: The Boston Retinal Implant Project. *Journal of Neuro-Ophthalmology,* Vol.32, (June 2011), pp. 160-168, ISSN 1070-8022.

Rodger, D. C.; Weiland, J. D.; Humayun, M. S. & Tai, Y.-C. (2005). Scalable Flexible Chip-level Parylene Package for High Lead Count Retinal Prostheses. *Proceedings of the 13th International Conference on Solid-State Sensors, Actuators and Microsystems*, ISBN 0-7803-8994-8, Seoul, South Korea, June 2005.

Rodger, D.C.; Weiland, J.D.; Humayun, M.S. & Tai, Y.C. (2006), Scalable High Lead-count Parylene Package for Retinal Prostheses. *Sensors and Actuators B: Chemical*, Vol. 117, (September 2006), pp. 107-114, ISSN 0925- 4005.

Rodger, D.C.; Fong, A.J.; Li, W.; Ameri, H.; Ahuja, A.K.; Gutierrez, C.; Lavrov, I.; Zhong, H.; Menon, P.R.; Meng, E.; Burdick, J.W.; Roy, R.R.; Edgerton, V.R.; Weiland, J.D.; Humayun, M.S. & Tai, Y.C. (2008). Flexible Parylene-based Multielectrode Array Technology for High-density Neural Stimulation and Recording. *Sensors and Actuators B: Chemical*, Vol. 132, (June 2008), pp. 449-460, ISSN 0925- 4005.

Stieglitz, T.; Haberer, W.; Lau, C. & Goertz, M. (2004). Development of an Inductively Coupled Epiretinal Vision Prosthesis. *Proc. Int. IEEE Eng. in Med. and Biol. Soc. Meet.*, ISBN 0-7803-8439-3, San Francisco, CA, USA, September 2004.

Tai, Y.C.; Rodger, D.C.; Li, W. & Tooker, A. (2006). *Method for Decreasing Chemical Diffusion in Parylene and Trapping at Parylene-to-parylene Interfaces*, US Patent Applicatio 11/408809. Available from
http://www.freepatentsonline.com/y2006/0255293.html

Tropepe, V.; Coles, B.L.K.; Chiasson, B.J.; Horsford, D.J.; Elia, A.J.; Mclnnes, R.R. & Kooy, D.V.D. (2000). Retinal Stem Cells in the Adult Mammalian Eye. *Science*, Vol. 287, (March 2000), pp. 2032-2036, ISSN 1934-7391.

Wong, Y.T.; Chen, S.C.; Seo, J.M.; Morley, J.W.; Lovell, N.H. & Suaning, G.J. (2009). Focal Activation of the Feline Retina via a Suprachoroidal Electrode Array. *Vision Research,* Vol 49, (May 2009), pp. 825-833, ISSN 0042-6989.

Weiland J.D. & Humayun, M.S. (2008). Visual Prosthesis. *Proceedings of the IEEE*, Vol. 96, (July 2008), pp. 1076-1084, ISSN 0018-9219.

World Health Organization. (2011). Prevention of Blindness and Visual Impairment. Available from http://www.who.int/blindness/causes/priority/en/index.html.

Wu, C.; Tang, C. & Liu, S. (2003). Analysis of On-chip Spiral Inductors Using the Distributed Capacitance Model. *IEEE J. of Solid-State Circuits*, Vol. 38, (June 2003), pp. 1040-1044, ISSN 0018-9200.

Wu J. (2003). *Inductive Links with Integrated Receiving Coils for MEMS and Implantable Applications* PhD thesis, University of Notre Dame. Available from
http://etd.nd.edu/ETD-db/theses/available/etd-09302003-162720/.

Zrenner, E.; Stett, A.; Weiss, S.; Aramant, R.B.; Guenther, E.; Kohler, K.; Miliczek, K.-D.;
          Seiler, M.J. & Haemmerle, H. (1999). Can Subretinal Microphotodiodes Successfully
          Replace Degenerated Photoreceptors? *Vision Research*, Vol. 39, (July 1999), pp. 2555-
          2567, ISSN 0042-6989.
Zolfaghari, A. Chan, A. & Razavi, B., Stacked Inductors and Transformers in CMOS
          Technology. *IEEE J. of Solid-State Circuits*, Vol. 36, (April 2001), pp. 620-628, ISSN
          0018-9200.
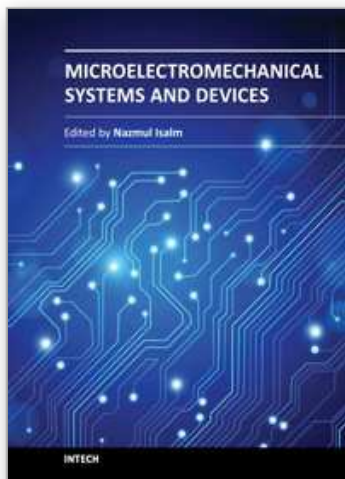
Microelectromechanical Systems and Devices

Edited by Dr Nazmul Islam

The advances of microelectromechanical systems (MEMS) and devices have been instrumental in the demonstration of new devices and applications, and even in the creation of new fields of research and development: bioMEMS, actuators, microfluidic devices, RF and optical MEMS. Experience indicates a need for MEMS book covering these materials as well as the most important process steps in bulk micro-machining and modeling. We are very pleased to present this book that contains 18 chapters, written by the experts in the field of MEMS. These chapters are groups into four broad sections of BioMEMS Devices, MEMS characterization and micromachining, RF and Optical MEMS, and MEMS based Actuators. The book starts with the emerging field of bioMEMS, including MEMS coil for retinal prostheses, DNA extraction by micro/bio-fluidics devices and acoustic biosensors. MEMS characterization, micromachining, macromodels, RF and Optical MEMS switches are discussed in next sections. The book concludes with the emphasis on MEMS based actuators.

How to reference

In order to correctly reference this scholarly work, feel free to copy and paste the following:

Wen Li, Damien C. Rodger, James D. Weiland, Mark S. Humayun, Wentai Liu and Yu-Chong Tai (2012). Implantable Parylene MEMS RF Coil for Epiretinal Prostheses, Microelectromechanical Systems and Devices, Dr Nazmul Islam (Ed.), ISBN: 978-953-51-0306-6, InTech, Available from:
http://www.intechopen.com/books/microelectromechanical-systems-and-devices/implantable-parylene-mems-rf-coil-for-epiretinal-prostheses

INTECH

open science | open minds